

# Structural Design and Aeromechanical Analysis of Unconventional Blades for Future Mars Rotorcraft

Ravi Lumba<sup>1</sup>, Cheng Chi<sup>1</sup>, Anubhav Datta<sup>1</sup>,  
Witold Koning<sup>2</sup>, Natalia Perez Perez<sup>2</sup>, and Haley Cummings<sup>2</sup>

<sup>1</sup>Alfred Gessow Rotorcraft Center, The University of Maryland at College Park

<sup>2</sup>Aeromechanics Branch, NASA Ames Research Center

## ABSTRACT

The structural design for rotor blades with thin, unconventional airfoils for Earth-based testing is obtained using three-dimensional (3D) aeromechanical analysis. This analysis is in support of the NASA ROAMX project. The outer mold was provided by NASA, but the internal structural design was developed at the University of Maryland and is presented here, along with a thorough aeromechanical analysis. The main objectives are to verify the structural integrity of the design and understand the unique aeroelastic behavior of the non-conventional airfoils designed for low-Reynolds number and high-Mach number flow. Six different blade models are considered, with the pitch axis varied from quarter-chord to mid-chord to determine the effect of C.G. offset on natural frequencies, blade deformations, root loads, and 3D stresses. All six blade designs are first studied under rotation in pure vacuum, and significant reductions in root loads and 3D stresses are achieved by moving the pitch axis closer to mid-chord to reduce the C.G. offset. Based on the vacuum analysis, the blade design with the pitch axis at 40% chord is selected for aerodynamic analysis. The blade control load, airloads, deformations, and 3D stresses are studied for steady hover. Dynamic control load and dynamic 3D stresses are studied for unsteady hover achieved using cyclic. Significant elastic twist is observed due to the trapeze effect and propeller moment, affecting the spanwise distribution of aerodynamic loads on the blades. However, the effect of aerodynamic loads on 3D stresses and the blade control load is found to be minimum. The dynamic control load is found to increase significantly due to inertial coupling from the C.G. offset. The dynamic stresses also increase, although still have factors of safety greater than two for both tensile and compressive stress.

## INTRODUCTION

On April 19, 2021, the Mars Helicopter (MH) Ingenuity demonstrated the first powered flight on another planet, opening a new era in Aeronautics and Mars exploration. The dream of rotorcraft flight on Mars (Refs. 1–3) was realized.

The 1.8 kg MH is a technology demonstrator with no payload, designed to inform our understanding of basic Martian aeronautics (Refs. 4, 5). Science missions will require larger platforms with longer endurance and greater payload. NASA and Jet Propulsion Laboratory have proposed follow-on conceptual designs with the University of Maryland conducting preliminary structural design of the rotor blades (Ref. 6). Two configurations were proposed – a coaxial and a hexacopter. They cover seven designs as presented in Table 1, with the MH listed for comparison. Two designs use coaxial rotors: a 4.6 kg Advanced Mars Helicopter (AMH) with the same rotor radius as MH and a 19.3 kg Mars Science Helicopter (MSH) with a rotor radius of 1.25 m. The other five designs are the hexacopters with a rotor radius of 0.64 m, each optimized for a different payload, range, and landing site.

Presented at the VFS Aeromechanics for Advanced Vertical Flight Technical Meeting, San Jose, CA, Jan 25-27, 2022. This is a work of the U.S. Government and is not subject to copyright protection in the U.S.

**Table 1. Family of next-generation Mars helicopter designs by NASA.**

Aircraft	Radius (m)	Mass (kg)	Payload (kg)
MH	0.605	1.8	0
AMH	0.605	4.6	1.3
MSH Coax	1.25	19.3	2.02
MSH Hexa Baseline	0.64	17.7	2.02
MSH Hexa Max cap(*)	0.64	31.2	0, 2, 5, 8
MSH Hexa Milankovic	0.64	17.12	2.1
MSH Hexa Becquerel	0.64	20.73	2.7
MSH Hexa Palikir	0.64	21.03	2.1

(\*) Maximum capacity of various ranges

The structural design and aeromechanical analysis of the MSH Hexa baseline was reported in Ref. 7. Sharp-edged, ultra-thin airfoils designed in Ref. 8 for low Reynolds number ( $Re$ ) were used. Significant twist deformations were observed, driven by the low torsional stiffness of the thin blades. Unlike conventional rotors, the elastic twist was not due solely to the propeller or aerodynamic moment, but the trapeze effect, which must be considered for ultra-thin blades. It was also observed that movement of the pitch axis was useful to re-

duce the loads without much adverse effect on stability. Both conclusions illustrated the unconventional behavior of these unique blades and the need for further studies.

To support the next generation of Mars rotorcraft, NASA recently launched the Rotor Optimization for the Advancement of Mars eXploration (ROAMX) project (Ref. 9). The ROAMX project seeks to develop an optimized Mars rotor using unconventional airfoils and rotor blades to significantly increase payload capacity, speed, and range for next-generation Mars rotorcraft. The approach consists of a computational and experimental investigation of Martian aerodynamics and dynamics.

The University of Maryland is one of the collaborators on the ROAMX project. Previous research (Refs. 8, 10–12) has shown that utilizing thin, unconventional airfoils can bring aerodynamic benefits in Mars. As part of this effort, the University of Maryland is researching the structural dynamics and aeroelastic behavior of such blades. The primary focus of this paper is on the structural design and aeroelastic analysis of a representative blade. The analysis uses a full 3D CAD-based description of the structure. Airloads, deformations, control loads, and 3D stresses are predicted. The placement of the pitch axis is also examined to reduce root loads and 3D stresses, similar to what was observed in Ref. 7.

## TECHNICAL APPROACH

The structural design of the blade is discussed before the detailed analysis begins. To observe the effect of the aeroelastic behavior, six different blade designs were developed, each with the pitch axis at different location between quarter-chord and half-chord. Next, a detailed 3D Finite Element Analysis (FEA) was carried out to investigate the natural frequencies, root loads, blade deformation, and 3D stresses due to rotation in vacuum. Based on the 3D stresses, a single blade design was chosen for the aeromechanical analysis. The blade was first studied in ideal hover, where the airloads, control load, and 3D stresses are presented. Finally, a cyclic is added to the blade in hover, and the dynamic stresses are studied to verify that the blades are able to handle small perturbations present in experimental hover testing. The airfoil decks needed in the analysis are provided by NASA. Throughout the paper particular attention is paid to the influence of the trapeze effect and the effect of moving the pitch axis back from the conventional location at the quarter chord toward mid-chord.

## TOOLS

The CAD designs were constructed in CATIA, and the flexible parts of the design were meshed in Cubit with higher order hexahedral elements. The connection between flexible parts and connections to the rest of the hub are modeled as multibody joints. The analysis is performed using the US Army/University of Maryland code X3D (Refs. 13, 14). X3D uses lifting line aerodynamics with C81 airfoil decks and has a built in 1D to 3D aerodynamic-to-structures interface. The interface was verified under Martian conditions by the authors in (Ref. 12) for a ultra-thin rotor tested in hover in a vacuum chamber.

## STRUCTURAL DESIGN

The rotor in this study is a four-bladed hingeless rotor with a radius of 0.72m and a geometric solidity of  $\sigma = 0.12$ . The main structural design goal was for the blade to withstand tip Mach numbers ranging from 0.7 up to 0.95 for Earth air composition at reduced pressures ( 18 mbar). Six different blade designs were developed and analyzed. The first one was a baseline design with the pitch axis located at the quarter chord. Due to low Lock number, leading-edge weights are not needed for stability. However, the resultant large chordwise center of gravity (C.G.) offset generates high root loads that may increase the weight of the hub and control system. Therefore five other designs – with the pitch axis varied from 30% to 50% chord in increments of 5% – were considered. Figure 1 shows the geometry for the two extremes – pitch axis at quarter-chord and mid-chord.

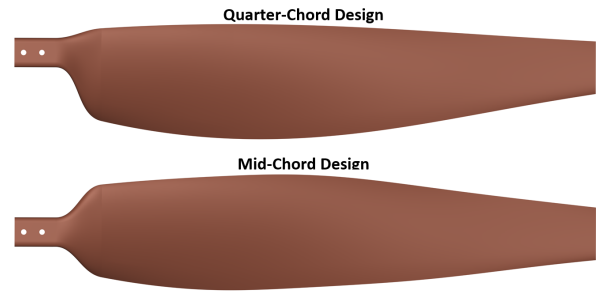


**Figure 1. Blade CAD models with pitch axis at quarter-chord and mid-chord.**

A highly cambered airfoil with a t/c of 6% is used at 25%R. From 50%R to the tip, the airfoils are ultra-thin, with a t/c of 1% as introduced in Ref. 8. Figure 2 shows the internal blade structure. The structural design was done to minimize weight while ensuring a sufficient factor of safety and considering manufacturability. The root insert is made of 7075 aluminum, starting at  $r/R = 12\%$  and ending at  $r/R = 18\%$ . From 18% to 35% there is a foam core made of Rohacell 31F foam. Surrounding the root insert and foam is the spar, which consists of NB 304-1 3K unidirectional tape. The spar starts at the root insert with 3 plies, with a 1 ply drop-off between  $r/R = 25\%$  and  $r/R = 35\%$ . The skin consists of carbon fiber NB 304-1 3K Bi-D  $\pm 45$  weave. There are 6 layers of skin at the root insert, with a 2 ply drop-off in the transition region to 25% and an additional 2 ply drop-off until 35%. Outboard of the spar ending at 45%, the blade is entirely skin. Table 2 presents the material properties for the spar and skin, obtained from the manufacturer. One interesting observation is that the  $E_1$  of the skin is close to that of the spar. This, coupled with the higher curvature found in the skin causes the skin to carry the highest stresses.

The chordwise C.G location is presented in Figure 3, and is located close to mid-chord. This is true even though the airfoils are not symmetric because the skin and spar account for 99% of the weight (not including the root insert) and are equally distributed around the blade. The C.G. offset is changed

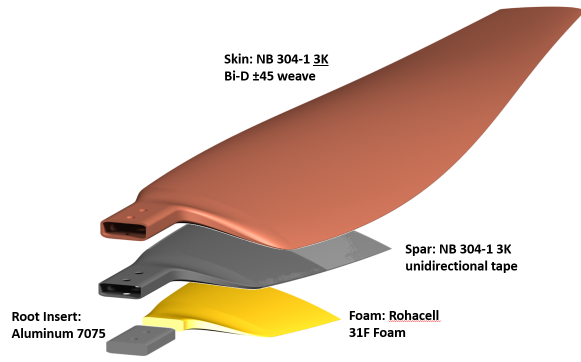


**Figure 2. Materials and internal structure of the blade design.**

**Table 2. Composite Material Properties**

Property	Skin	Spar
Density ( $\text{kg/m}^3$ )	1480	1550
$E_1$ (GPa)	89.63	114.45
$E_2$ (GPa)	89.63	6.8
$G_{12}$ (GPa)	4.137	4.137
$\nu_{12}$	0.05	0.29

through movement of the pitch axis location, and is nearly eliminated with the mid-chord design.

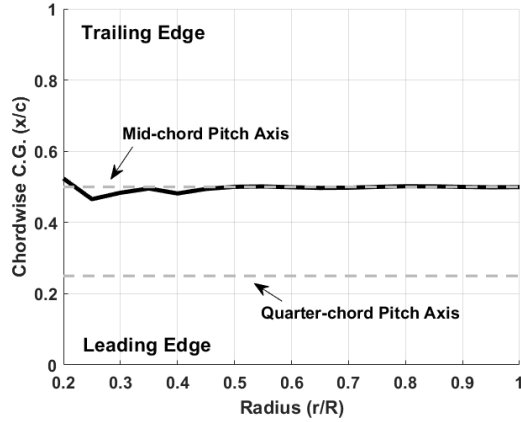


**Figure 3. Chord-wise C.G. location.**

In addition to the blade, a significant portion of this work involved designing a blade adapter to connect the blade to the hub structure. However, due to their proprietary nature, both the blade adapter and the hub structure cannot be shown in the paper.

### 3D Structural Model

The blade and blade adapter are meshed separately but connected through multibody joints and analyzed together. The meshes for the quarter-chord and mid-chord blade designs are presented in Figure 4. All 6 designs have 20,455 nodes and 2,237 higher-order 27-noded hexahedral brick elements. The blade adapter has 6,880 nodes and 616 higher-order 27-noded

hexahedral brick elements, bringing the total number of degrees of freedom for the system to approximately 75K.

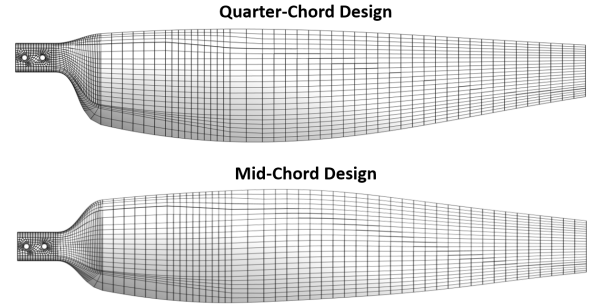


**Figure 4. Blade meshes with pitch axis at quarter-chord and mid-chord.**

There are five multibody joints present in the analysis, used to model the connections between physical parts and simulate the load path. There are two bolt holes that connect the blade and blade adapter, as seen in Figure 5. Both of these connections are modeled as separate joints with all degrees of freedom locked, meaning that the two bodies (blade and blade adapter) can have no relative motion at these points. All of the loads from the blade flow into the blade adapter through the two joints. The other three joints connect the blade adapter to the hub, and are constructed to match the physical load path.

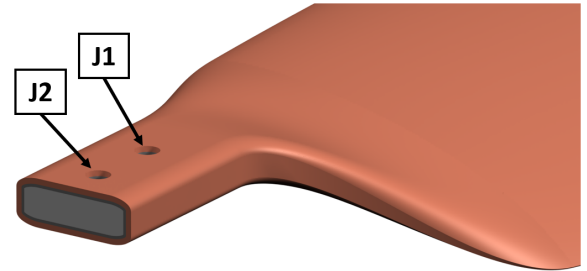


**Figure 5. The two bolt holes that connect the blade and blade adapter are modeled as individual joint connections J1 and J2.**

### ROTATION IN VACUUM

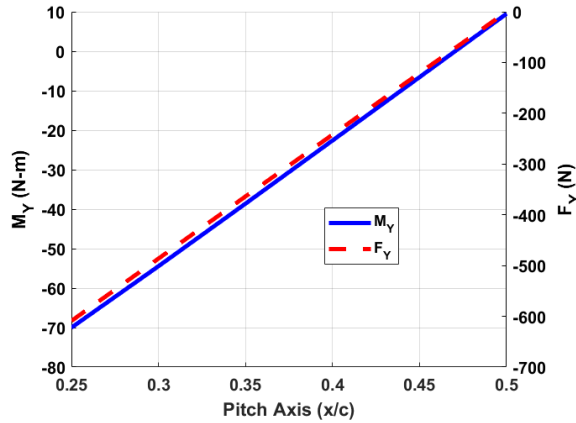
This section studies the structural response in vacuum. The root loads, blade deformations, 3D stresses, and natural frequencies due to rotation in vacuum are presented. Based on the stresses in the blade, and to minimize the stresses in the blade adapter, one blade design will be chosen to continue the aerodynamic analysis. Studying the behavior of the ultra-thin blades in vacuum is important, as it allows for a greater understanding of the inertial coupling caused due to unique blade design and pitch axis location without the complications of aerodynamics.

### Blade Root Loads

In this section, the blade root loads are studied for different pitch axis locations and collectives to observe the effect of in-

plane and out-of-plane C.G. offset. The tip Mach number for these cases was 0.95, the highest for which the analysis was conducted, as it will produce the highest loads. The lead-lag force, blade torsional moment, and blade flapping moment are studied, as these loads are most affected by the relocation of the pitch axis (effectively reducing the C.G. offset). The sign convention for the root loads is as follows: the lead-lag force ( $F_Y$ ) is positive toward the leading edge, the torsional moment ( $M_X$ ) is positive nose-up, and the bending moment ( $M_Y$ ) is positive flap down.

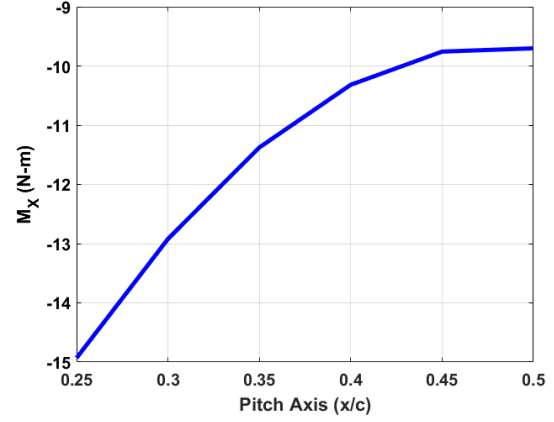
The lead-lag force and blade flapping moment for varying pitch axis locations are presented in Figure 6 for a case with a collective of  $20^\circ$ . The blade C.G. remains close to the mid-chord along the entire radius (Figure 3), therefore, when the pitch axis is located at 25% chord the in-plane component of the centrifugal force causes a large lag force. The large C.G. offset has a similar effect on the blade flapping moment. For a high pitching angle and the pitch axis at quarter-chord, the blade C.G. drops below the plane of rotation, causing a large flap up moment. Both the lag force and blade flapping moment can be drastically reduced by moving the pitch axis to mid-chord, reducing the loads on the hub.



**Figure 6. Blade lead-lag force and blade flapping moment vs. pitch axis for a collective of  $20^\circ$ .**

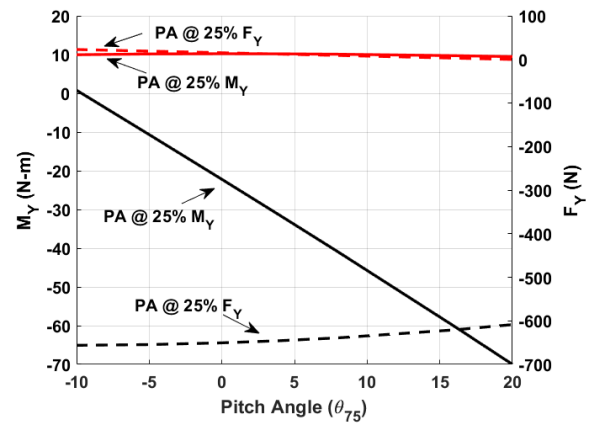
Figure 7 shows the blade torsional moment plotted against pitch axis for the same case presented above. Similar to before, the C.G. offset causes high loads when the pitch axis is located at quarter-chord, this time through the propeller moment. However, unlike for the lead-lag force and blade flapping moment, eliminating the C.G. offset will not bring the net load to zero. The high twist and rotational speed mean that a high propeller moment is still present, even with the pitch axis at mid-chord.

Figure 8 and 9 shows the same loads, but now the variation with collective is studied. Only the two extreme blade designs (pitch axis at 25% chord and pitch axis at 50% chord) are shown. It is clear that the lag force remains relatively constant with collective, as the lateral change in C.G. with moderate collective is negligible. The blade flapping moment however, seems to vary with collective, but only when the pitch axis is



**Figure 7. Blade pitching moment vs. pitch axis for a collective of  $20^\circ$ .**

at quarter-chord. The blade flapping moment is dependent on the out-of-plane C.G. offset, which is large when the pitch axis is at quarter chord and the collective is high. However, the total C.G. offset is very small for pitch axis at mid-chord, and therefore the out-of-plane C.G. offset does not change much with collective. The blade torsional moment decreases with collective due to the reduction in propeller moment. Overall, it is seen that moving the pitch axis toward mid-chord can significantly reduce the blade torsional moment by up to 35% and can almost eliminate the in-plane root shear and blade flapping moment. The reduction in torsional moment is important as it reduces the pitch link loads and allows for lighter servos. Previous designs required counterweights to alleviate the pitch bearing loads, so moving the pitch axis will reduce the weight penalty of the counterweights or eliminate the need for them entirely.



**Figure 8. Blade lead-lag force and blade flapping moment vs.  $\theta_{75}$  for pitch axis at quarter-chord and mid-chord.**



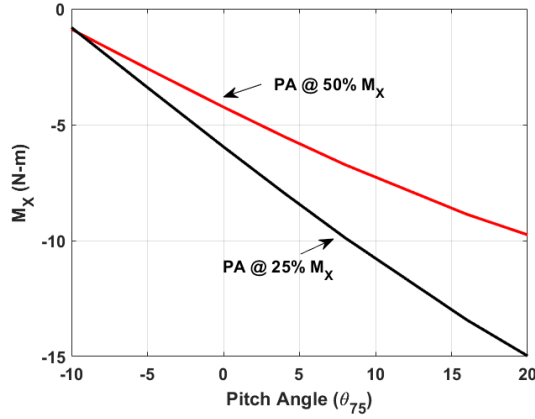


**Figure 9. Blade pitching moment vs.  $\theta_{75}$  for pitch axis at quarter-chord and mid-chord.**

### Blade Deformation

Previous work by the authors (Ref. 7) found that the elastic twist deformations are very high for ultra-thin blades, due to a combination of the high propeller moment, trapeze effect, and extremely low torsional stiffness. The trapeze effect will always try to untwist the blade and is dependent on the twist. The propeller moment will try to flatten the blade relative to the local chord line and is dependent on the local pitch angle (higher the pitch angle, higher the propeller moment). Understanding the interaction between the propeller moment and the trapeze effect for different collectives is paramount to properly designing an efficient blade. Again, the results for this section are obtained for a tip Mach number of 0.95, as this will yield the highest deformations.

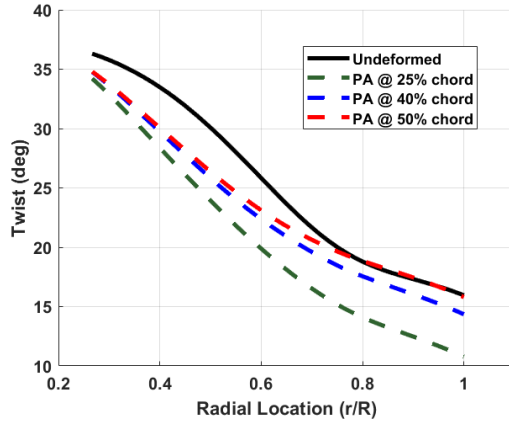


**Figure 10. Blade elastic twist in vacuum at  $\theta_{75} = 20^\circ$ .**

Figure 10 shows the blade twist versus span for a collective of  $20^\circ$ . Three different blade designs are shown. There are two key conclusions that can be drawn. First, the blade has significant elastic twist occurring before the blade starts – this occurs in the transition region and is due to the high propeller moment caused by the high pitch angle. Second, the deformations vary considerably with pitch axis location. When the

pitch axis is at 25% chord, the propeller moment is very high (shown in the previous section). This causes the blade to twist down significantly near the tip. However, when the pitch axis is moved to mid-chord, there is little elastic twist at the tip. For the inboard section of the mid-chord case, the propeller moment still causes a twist down due to a high twist angle. However, at the outboard section the lower pitch angle reduces the propeller moment enough to where it is balanced by the trapeze effect, causing little elastic twist.

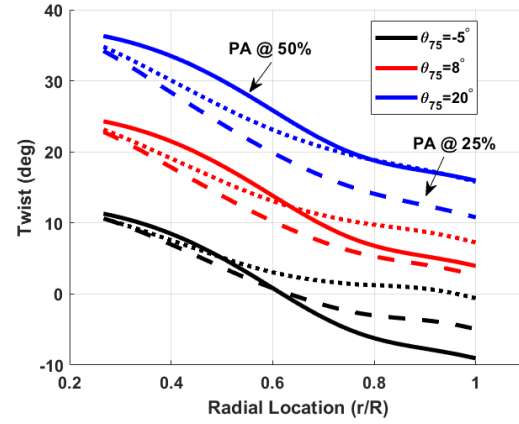


**Figure 11. Blade elastic twist for rotation in vacuum at different collectives. Dashed lines are pitch axis at quarter-chord and dotted lines are pitch axis at mid-chord.**

Figure 11 shows the blade twist versus span for three different collectives and two blade designs. For each collective, the interaction between the trapeze effect and propeller moment is different. For the lowest collective of  $-5^\circ$ , the propeller moment is very small due to the low pitch angle. Near the tip the local pitch angle is less than zero, so the propeller moment is working with the trapeze effect to untwist the blade, causing significant pitch deformations of approximately  $10^\circ$ . For a moderate collective of  $8^\circ$ , the propeller moment and trapeze effect appear to be almost balanced for the quarter-chord design. However, since the mid-chord design has a significantly lower propeller moment, the trapeze effect causes it to twist up near the tip. As mentioned previously, at a collective of  $20^\circ$ , the mid-chord design has little elastic twist near the tip, while the quarter-chord design has significantly higher propeller moment causing significant nose down twist. Overall, moving the pitch axis backward from quarter-chord will cause the blade to twist up (in reference to the quarter-chord design) from the decreased propeller moment. The significant elastic twist means that flexibility must be considered when performing aerodynamic analysis.

### 3D Stress

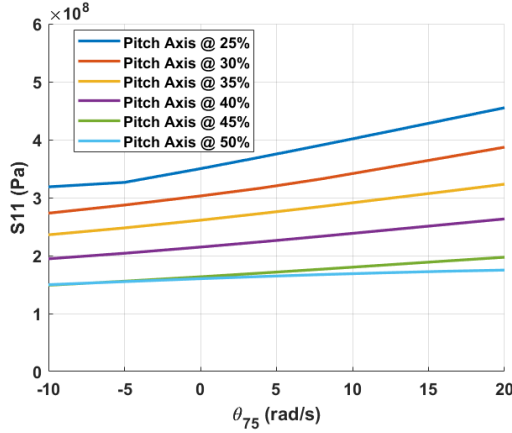
Three-dimensional FEA allowed the direct examination of 3D stresses, which were used to evaluate the factor of safety of the design. The maximum tensile and compressive stresses were evaluated for the blade to determine the factors of safety. For

all cases in this section, the tip Mach number is 0.95 used to produce the highest loads. The tensile and compressive strength for the materials is given in Table 3.

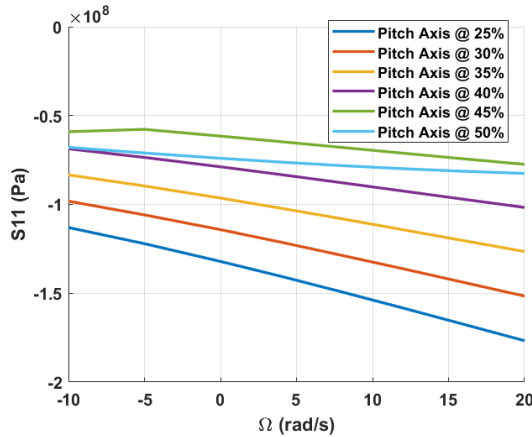
**Table 3. Composite Material Strength Properties**

Property	Skin	Spar
Tensile Strength (GPa)	586	1992
Compressive Strength (GPa)	467	951

Figure 12 shows the maximum tensile stress in the blade versus pitch angle for different blade designs. The stresses vary considerably with both pitch axis location and collective. The trends appear to be similar to that of the torsional moment shown previously (Figure 7 and 9), in that moving the pitch axis to mid-chord and decreasing the pitch angle reduce the maximum loads on the blade.



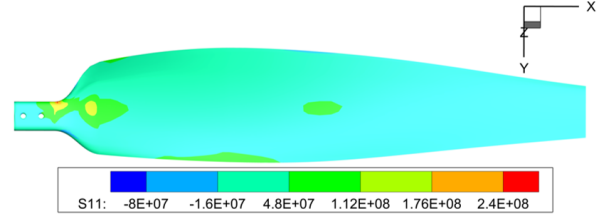
**Figure 12. Maximum stress in blade for different collectives and blade designs.**



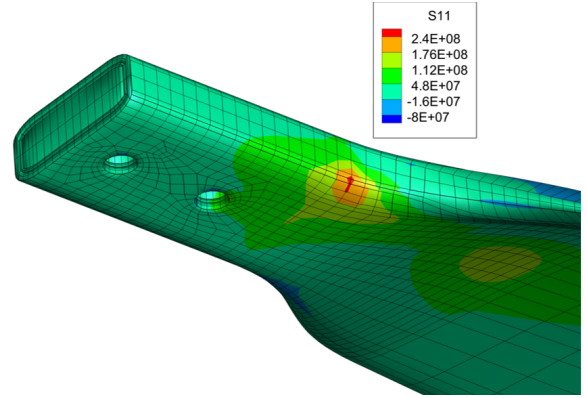
**Figure 13. Minimum stress in blade for different collectives and blade designs.**

Figure 13 shows the maximum compressive stress in the blade versus pitch angle for different blade designs. Similar to the maximum tensile stress, the compressive stresses vary with

both pitch axis location and collective, with the maximum stresses when the pitch axis is at quarter-chord and the collective is high.



**Figure 14. Blade axial stress ( $\sigma_{11}$ ) at the bottom surface for a collective of 20° and pitch axis of 40 percent chord.**



**Figure 15. Blade axial stress ( $\sigma_{11}$ ) near the root for a collective of 20° and pitch axis of 40 percent chord.**

Figure 14 and 15 show the blade axial stress for a collective of 20° for the design with the pitch axis the 40% chord. The bottom view of the blade shows highly localized stress patterns close to the root, due to the high curvature of the transition region. From Figure 15 it is clear that the maximum stress occurs at the inboard transition section near the TE. One other interesting note is that the maximum stress occurs in the skin rather than the spar, likely due to the higher curvature for the skin. Figure 16 shows the location of the maximum compressive stress for a collective of 20° for the design with the pitch axis the 40% chord. The highest compressive stress occurs in the skin around the forward bolt hole that attaches the blade to the blade adapter. A large portion of the stress is caused by the steady axial CF, but some is due to moments and shear force caused by the C.G. offset. This results in the stress concentration shifting toward the TE of the bolt hole and varying with both pitch axis and collective.

Table 4 and 5 present the maximum tensile and compressive stresses and factors of safety for each blade design. The factor of safety for the tensile stress is much lower than the compressive stress, so those results were used to drive the design choice. To purely minimize tensile stress, the mid-chord pitch axis design would be selected. However, placing the pitch axis at mid-chord drastically reduces the pitch damping. Therefore, a pitch axis location of 40% was chosen as a balance between stresses (factor of safety of over 2) and stability.

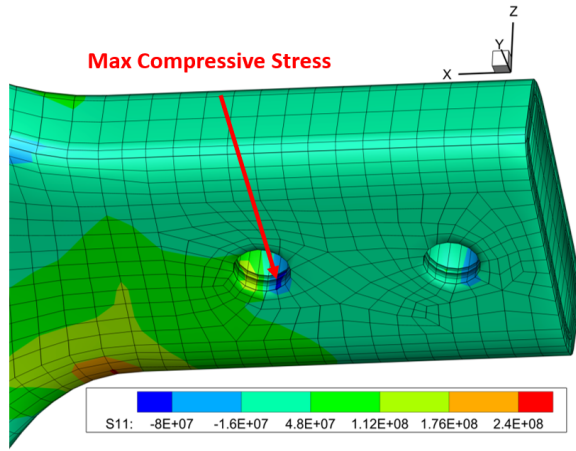


**Figure 16. Blade axial stress ( $\sigma_{11}$ ) near the blade adapter connection for a collective of  $20^\circ$  and pitch axis of 40 percent chord.**

**Table 4. Max Tensile Stress versus Pitch Axis.**

Pitch Axis	Maximum Tensile Stress (MPa)	FoS
25% chord	455	1.29
30% chord	387	1.51
35% chord	323	1.81
40% chord	263	2.23
45% chord	197	2.97
50% chord	175	3.34

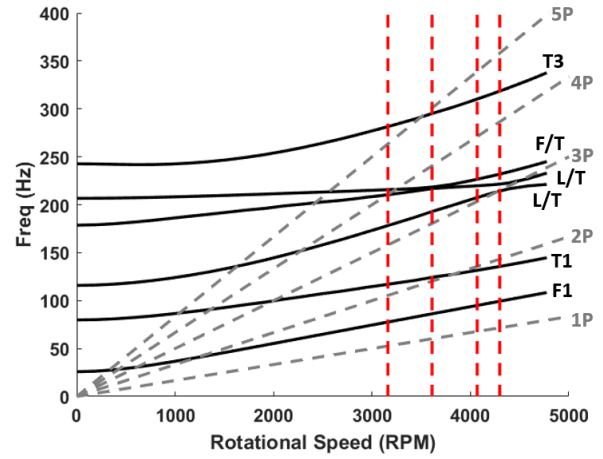
**Table 5. Max Compressive Stress versus Pitch Axis.**

Pitch Axis	Maximum Compressive Stress (MPa)	FoS
25% chord	177	2.64
30% chord	152	3.07
35% chord	127	3.68
40% chord	102	4.58
45% chord	77	6.06
50% chord	82	5.70

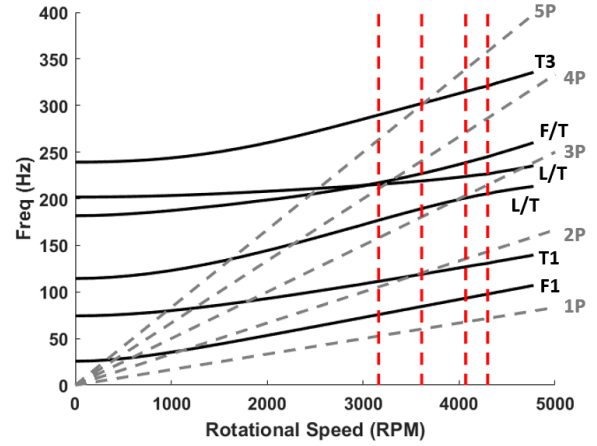
## Natural Frequencies

Figure 17 shows the fan plot for the selected blade design (pitch axis at 40 % chord). The four vertical lines indicate tip Mach numbers of 0.7, 0.8, 0.9, and 0.95, which are the preliminary values for testing. Figure 18 shows the fan plot for the baseline blade design (pitch axis at 25 % chord) for reference.

For both blade designs, the first two modes are clear flap and torsion respectively, as seen in Figure 19 and 20 for the 40% blade design (quarter-chord design is almost identical). However, all higher modes have significant coupling due to the large CG offset. For example, the 3rd mode for both models is a coupled lag-torsion mode, and is shown in Figure 21 for the 40% pitch axis model. This indicates that despite reducing the C.G. offset, there is still significant torsion coupling with both flap and lag. The cause of this coupling is twofold. The C.G. offset, which remains about 10% of the chord, will still cause a significant coupling of the modes. Additional coupling is due to the low torsional stiffness and trapeze effect,



**Figure 17. Fan Plot for Pitch Axis at 40 % chord.**



**Figure 18. Fan Plot for quarter-chord design.**

which causes high torsional deformations due to the high rotational speed. For the design with the pitch axis at 40%, the third mode is close to 3/rev for the highest tip Mach number case. This should be watched carefully moving forward, but will likely change when the control system stiffness is finalized.

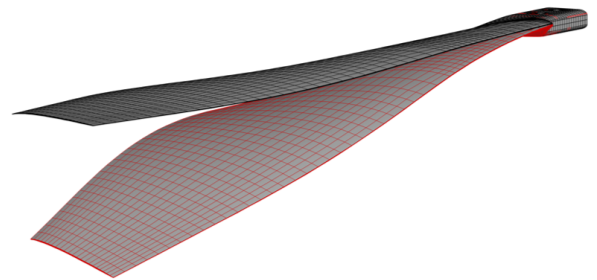


**Figure 19. First Flap for blade with pitch axis at 40 percent chord and a tip Mach number of 0.95. The gray and red blades are undeformed and deformed respectively.**

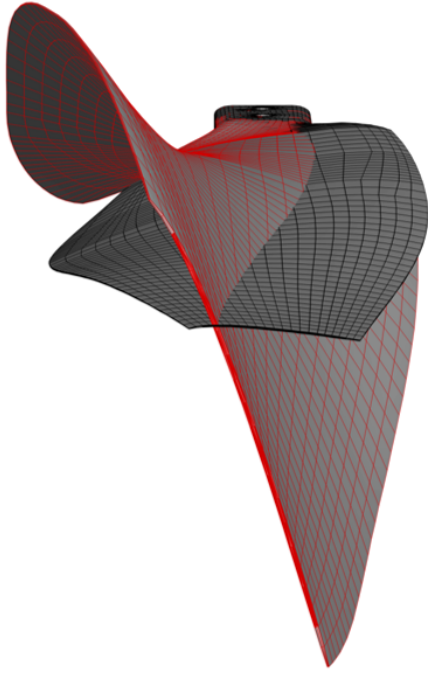


**Figure 20. First torsion for blade with pitch axis at 40 percent chord and a tip Mach number of 0.95. The gray and red blades are undeformed and deformed respectively.**

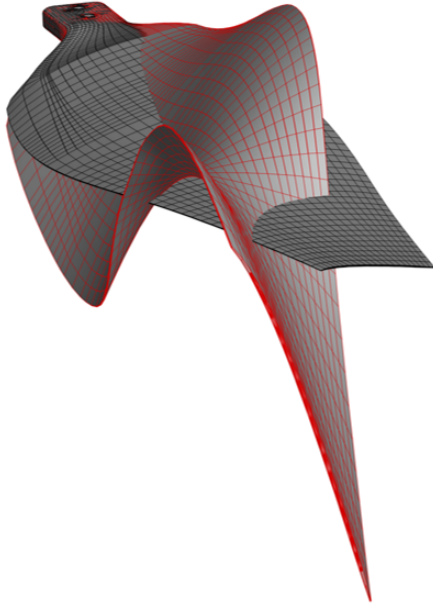


**Figure 21. Third mode (coupled torsion-lag) for blade with pitch axis at 40 percent chord and a tip Mach number of 0.95. The gray and red blades are undeformed and deformed respectively.**

## IDEAL HOVER

Hover analysis is performed over a range of collective pitch angles from  $-8^\circ$  to  $20^\circ$  in increments of  $1^\circ$ . The effect of aerodynamics on the blade control load is examined. Next, the effect of flexibility and sectional deformations on sectional airloads is presented. Finally, the 3D stresses are studied. As

part of the hover analysis, rotor parameters such as blade loading ( $C_T/\sigma$ ), power loading ( $C_P/\sigma$ ), and figure of merit were studied. However, these values are not able to be released, so are not published here. The atmospheric conditions used are those found at the Planetary Aeolian Laboratory (PAL) where the ROAMX blades are to be tested (Ref. 9). Table 6 compares these conditions to nominal Earth values.

**Table 6. Atmospheric Conditions.**

Parameters	Earth (SL/ISA)	Earth (PAL)
Density ( $\text{kg/m}^3$ )	1.225	0.015
Speed of Sound (m/s)	343	341
Dynamic Viscosity ( $\text{Ns/m}^2$ )	$1.75 \times 10^5$	$1.75 \times 10^5$

## Blade Aerodynamic Model

The blade was divided up into 18 aerodynamic segments, each with its own unique airfoil, Mach number ( $M$ ), and Reynolds number ( $Re$ ). The aerodynamic segments are shown in Figure 22. The aerodynamics in the transition region were neglected, as the dynamic pressure will be very small. For each segment, the aerodynamic forces are calculated and applied to all surface nodes within that segment. Each region has its own C81 airfoil deck provided by NASA. For each deck, the aerodynamic coefficients are functions of angle of attack and Mach number with a fixed  $Re/M$  ratio. Within each region, fine tuning to the local Reynolds number was based on standard correction (Ref. 15).

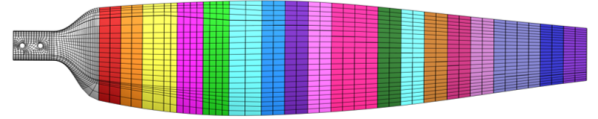


**Figure 22. The blade aerodynamic segments are shown. Aerodynamics was neglected in the transition region.**

## Control Load

This section studies the effect of aerodynamics on the root torsional moment (control load). This is the load that the pitch control actuator will have to handle, and therefore is crucial in the design process. Figure 23 presents the variation of blade torsional moment with blade loading. Most of the load is due to the inertial propeller moment, so the total moment has a similar trend as pure rotation in vacuum. Despite the location of the pitch axis behind the aerodynamic center, the net aerodynamic moment is nose-down, although the magnitude is significantly less than the inertial moment. Therefore, the magnitude of the total control moment is slightly higher with aerodynamics than in vacuum. The large control load will be handled by using large actuators. For when weight-saving is crucial, counterweights can be used to reduce the control load to a manageable level. Though it is possible, including counterweights was not pursued in this effort.



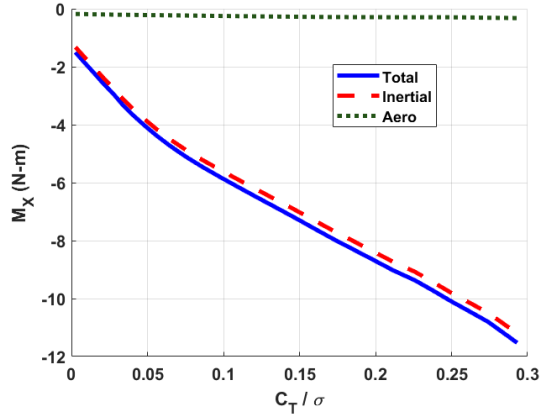
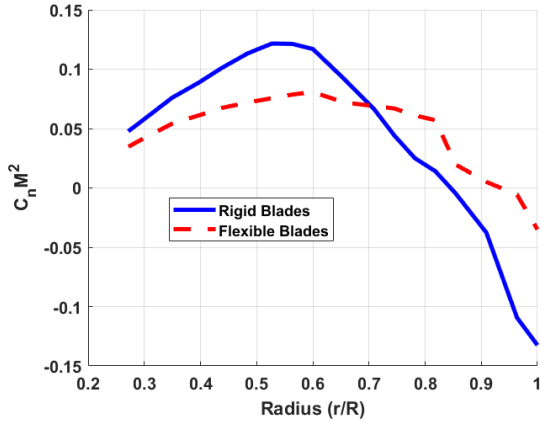


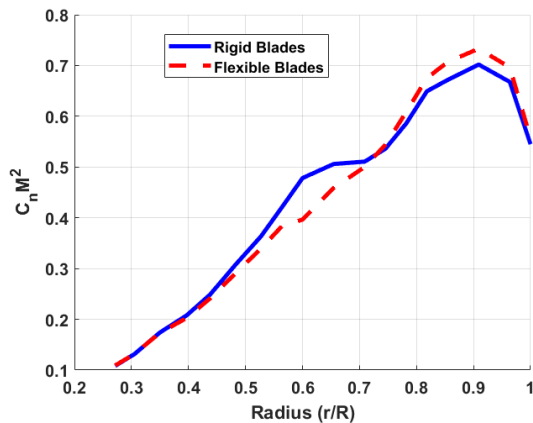
Figure 23. Blade control load versus blade loading

### Sectional Airloads and Blade Deformations

This section presents the sectional spanwise airloads and blade deformations. The effect of flexibility on spanwise airloads is examined at a low ( $C_T/\sigma = 0.03$ ) and a high ( $C_T/\sigma = 0.25$ ) blade loading. Figure 24 shows the sectional normal force for the two cases, along with the different collectives for each case.



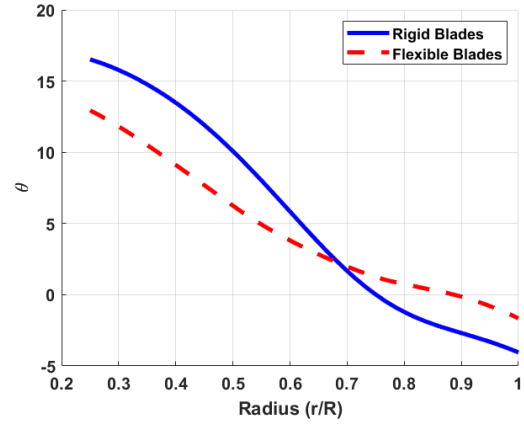
(a)  $C_T/\sigma = 0.03$ .  $\theta_{75} = 0^\circ$  for rigid blade and  $\theta_{75} = -3^\circ$  for flexible blade.



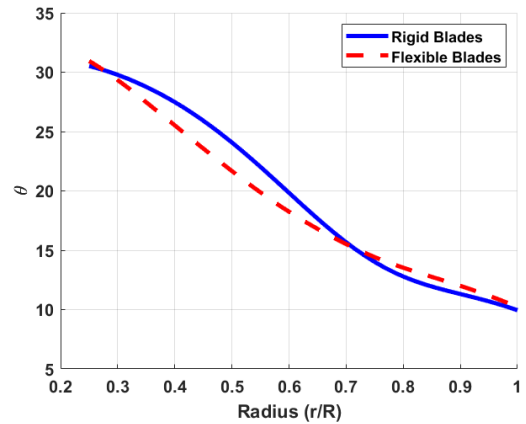
(b)  $C_T/\sigma = 0.25$ .  $\theta_{75} = 14^\circ$  for rigid blade and  $\theta_{75} = 16^\circ$  for flexible blade.

Figure 24. Hover sectional normal force.

The effect of flexibility on the spanwise loads distribution is significant. To further understand the difference in airloads, the elastic twist is shown for both cases in Figure 25. For the low blade loading case, significant pitch up elastic twist is seen. Despite a lower collective of 3 degrees, the flexible blade has a higher pitch from  $r/R = 0.7$  to the tip, matching the sectional airload trend shown in Figure 24(a). For the high blade loading case, the flexible blade has a lower pitch angle at the inboard sections, in spite of a two degree greater collective. However, the pitch down is less at the tip, where the flexible blade outproduces the rigid blade.



(a)  $C_T/\sigma = 0.03$ .  $\theta_{75} = 0^\circ$  for rigid blade and  $\theta_{75} = -3^\circ$  for flexible blade.



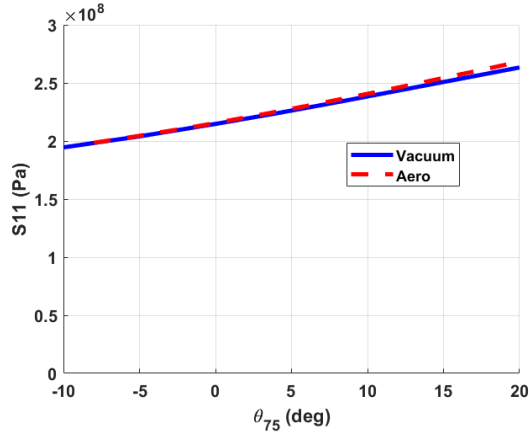
(b)  $C_T/\sigma = 0.03$ .  $\theta_{75} = 14^\circ$  for rigid blade and  $\theta_{75} = 16^\circ$  for flexible blade.

Figure 25. Hover sectional twist.

### 3D Stress

The 3D stresses were examined in the blade to determine the change in the factor of safety with the addition of aerodynamics. Figure 26 shows the maximum tensile stress in the blade versus pitch angle. For low collectives, there was no difference between the aerodynamics and pure rotation in vacuum. For high collectives, when the blade loading was at its maximum, there was a small increase in maximum tensile stress of about 2%. Figure 27 shows the maximum compressive stress in the blade versus collective. Similar to the maximum tensile stress, the addition of aerodynamics only makes a difference for high collectives, as this is when the C.G. offset has

a greater effect. The increase in maximum compressive stress is about 2% with aerodynamics for a collective of 20°.



**Figure 26. Comparison of maximum tensile stress in blade with and without aerodynamics.**

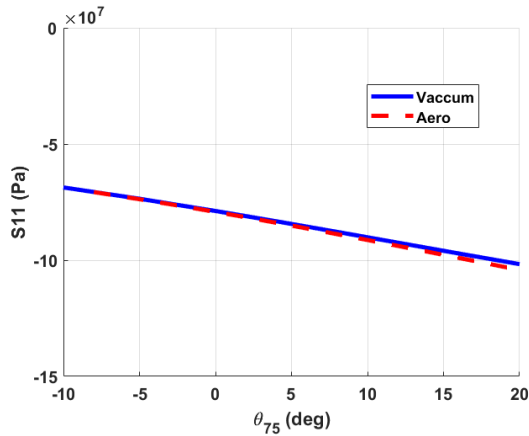


**Figure 27. Comparison of maximum compressive stress in blade with and without aerodynamics.**

Table 7 and 8 present the maximum tensile and compressive of the blade in both vacuum and with aerodynamics, along with the final factor of safety with aerodynamics for different pitch angles. Similar to pure rotation in vacuum, the factor of safety is much higher for compressive stress than for tensile stress. In steady hover with a collective of 20° the factors of safety for tensile and compressive stress are 2.19 and 4.49 respectively.

**Table 7. Max Tensile Stress with Aerodynamics.**

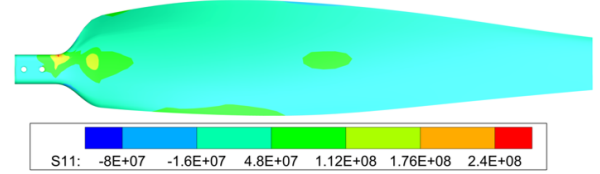
Collective	Vacuum $\sigma_{11}$ (MPa)	Aero $\sigma_{11}$ (MPa)	FoS
-5°	204	205	2.86
0°	215	216	2.71
8°	233	235	2.49
20°	263	268	2.19

Figure 28, 29, and 30 show the axial stress on the blade. Overall, the stress patterns look identical to rotation in vacuum, and the locations of maximum stress are the same for tensile and compressive stress. The almost negligible effect of aerodynamics on the blade stresses is due to the extremely low

**Table 8. Max Compressive Stress with Aerodynamics.**

Collective	Vacuum $\sigma_{11}$ (MPa)	Aero $\sigma_{11}$ (MPa)	FoS
-5°	74	74	6.31
0°	79	79	5.91
8°	88	89	5.25
20°	102	104	4.49

density and high rotational speed. The maximum thrust produced by one blade is less than 1% of the CF, so the loads and stresses are dominated by the inertial terms.



**Figure 28. Blade axial stress ( $\sigma_{11}$ ) with aerodynamics at the bottom surface for a collective of 20°.**

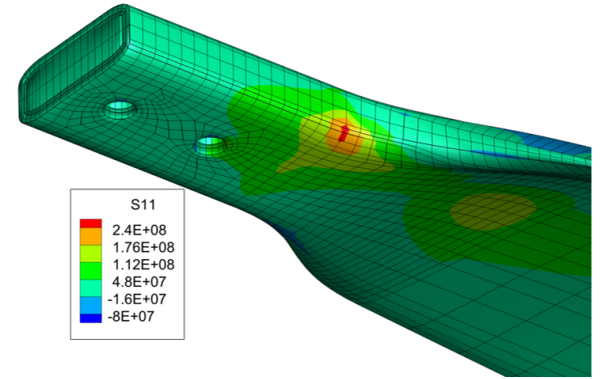


**Figure 29. Blade axial stress ( $\sigma_{11}$ ) with aerodynamics at the root for a collective of 20°.**

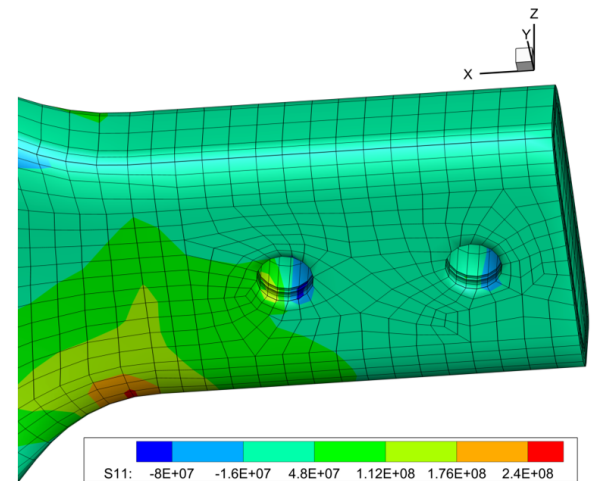


**Figure 30. Blade axial stress ( $\sigma_{11}$ ) with aerodynamics near the blade adapter connection for a collective of 20°.**

## HOVER WITH CYCLICS

This section studies the dynamic loads of the rotor in hover with cyclics applied. All the results in the previous section were obtained for ideal hover. However, during testing there will be perturbations and oscillations, caused by recirculation, small differences between the blades, or changes in the rotational speed. The low Lock number will cause these oscillations to damp out very slowly, requiring a high number of revolutions. Therefore, the maximum loads produced by these oscillations must be taken into account during the design process. The control load and dynamic 3D stress are needed to design the control actuators and blade. To simulate these perturbations, varying lateral cyclics were applied.

### Control Load

The oscillatory control load is presented in Figure 31 for a collective of  $20^\circ$  and lateral cyclics of  $1^\circ$ ,  $2^\circ$ , and  $5^\circ$ . As expected, the behavior for all cases is strongly 1/rev due to the cyclic. However, there is a phase shift of about  $90^\circ$  from what is expected. Based on the static propeller moment, the magnitude of  $M_X$  should be at a maximum at  $0^\circ$ , when the pitch angle is highest. The fact that there is a phase shift indicates that the inertial terms are dominating the oscillatory behavior, likely through the pitch-flap coupling due to the C.G offset. The influence of aerodynamic moment is assumed to be minimal based on Figure 23 from the previous section. Another indication that inertial terms are dominating is that the peak-to-peak is much higher than the change in torsional moment seen for steady hover (Figure 23 covered approximately 25 degrees and only varied by 10 N-m).

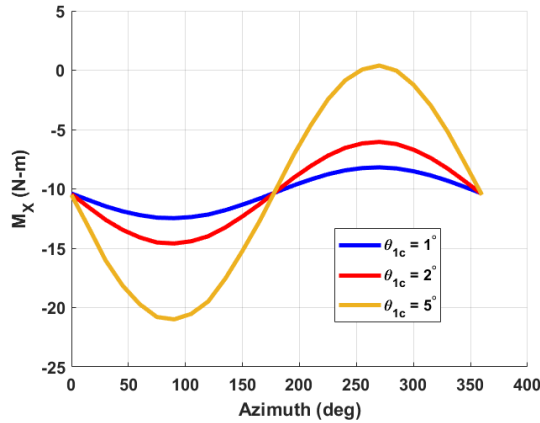


Figure 31. Oscillatory control load for a collective of  $20^\circ$  and lateral cyclics of  $1^\circ$ ,  $2^\circ$ , and  $5^\circ$ .

Figure 32 presents the torsional moment peak-to-peak versus collective for the different cyclic values. The amplitude seems to be steady with collective, and varies linearly with cyclic. Figure 33 shows the maximum control load versus collective for different lateral cyclics. Overall, the inertial forcing increases the loads significantly, although the propeller moment still makes up a substantial portion of control load. The actuator and pitch links must be sized to handle not just the high steady loads, but also the oscillatory loads that will be made more important by the low aerodynamic damping.

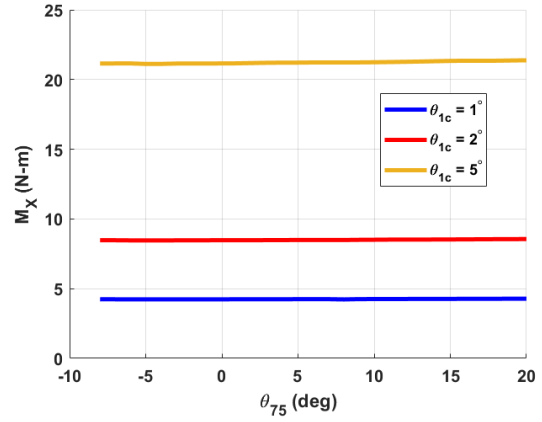


Figure 32. Oscillatory control load peak to peak versus collective for lateral cyclics of  $1^\circ$ ,  $2^\circ$ , and  $5^\circ$ .

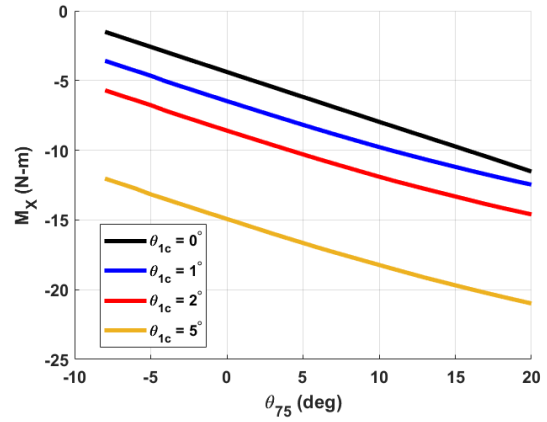


Figure 33. Maximum control load versus collective for lateral cyclics of  $1^\circ$ ,  $2^\circ$ , and  $5^\circ$ .

### Dynamic Stresses

Figure 34 and 35 show the maximum tensile and compressive stress for the blade versus azimuth for a collective of  $20^\circ$  and different lateral cyclics. As predicted, the behavior is dominated by 1/rev, and the largest cyclics produces the largest oscillatory stresses. The maximum values of the stresses occur at approximately  $45^\circ$  and  $225^\circ$ , offset from the maximum control moment by  $45^\circ$ .

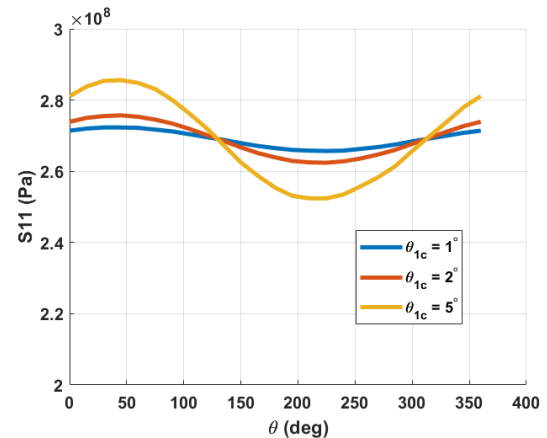


Figure 34. Maximum tensile stress in blade versus azimuth for lateral cyclics of  $1^\circ$ ,  $2^\circ$ , and  $5^\circ$ .

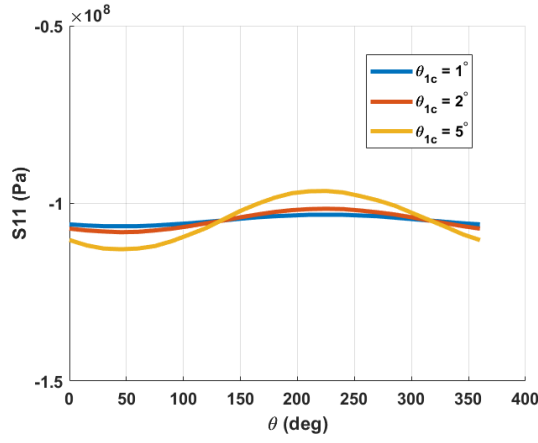


Figure 35. Maximum compressive stress in blade versus azimuth for lateral cyclics of  $1^\circ$ ,  $2^\circ$ , and  $5^\circ$ .

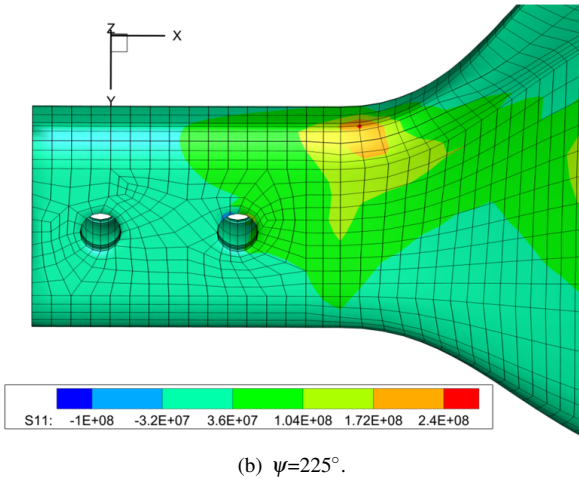
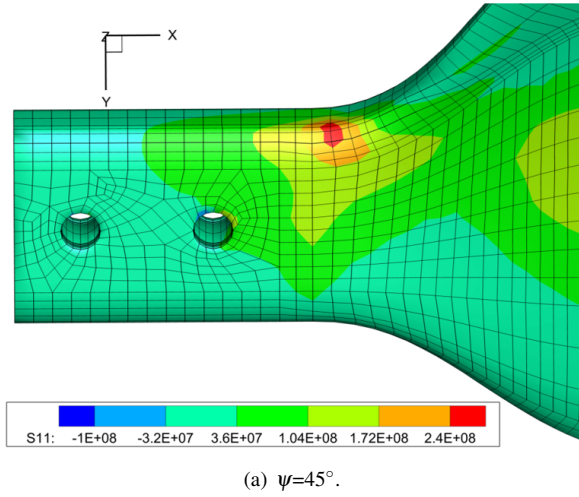
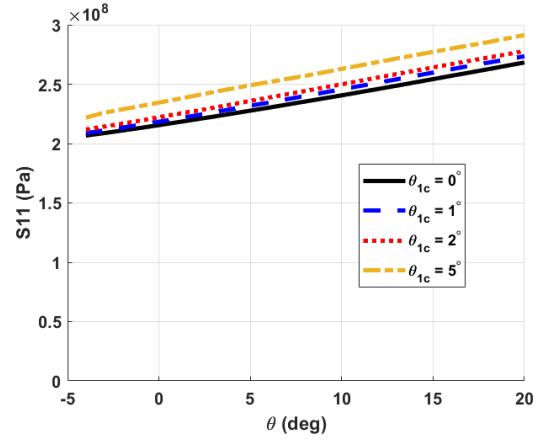
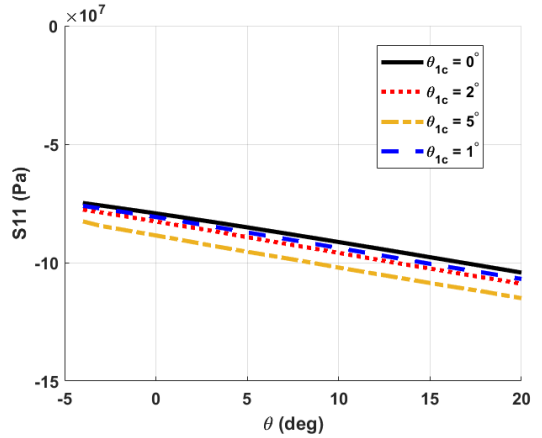


Figure 36. Axial Bending Stress for  $\theta_{75} = 20^\circ$  and  $\theta_{1c} = 5^\circ$

Figure 36 shows the stresses at the blade root at  $45^\circ$  and  $225^\circ$  with the highest lateral cyclic ( $\theta_{1c} = 5^\circ$ ). The maximum stresses occur in the same location as seen previously, however the magnitude and the localized stress pattern change with azimuth. Figure 37 shows the maximum tensile and compressive stresses present in the blade versus collective for various lateral cyclics. The addition of cyclics increases the maximum stresses through inertial forcing, but the steady CF forces still remain the dominant load. Both the maximum tensile and compressive stresses increase by approximately 10 %, to 291 MPa and 116 MPa respectively ( $\theta_{75} = 20^\circ$  and  $\theta_{1c} = 5^\circ$ ). This brings the final factors of safety to 2.01 and 4.03, still well within the material limits.



(a) Maximum Tensile Stress.



(b) Maximum Compressive Stress.

Figure 37. Maximum Tensile and Compressive Stress for different lateral cyclics.

## CONCLUSIONS

An aeromechanical analysis of rotor blades with extremely thin, unconventional airfoils was conducted in this paper in support of the NASA ROAMX program. The main objective was to create the internal structural design of the rotor blade and blade adapter to achieve sufficient factors of safety, as well as further study the aeroelastic behavior of these unique designs. Structural analysis in vacuum and comprehensive



analysis in both steady and unsteady hover was performed. Six different blade designs were considered, each with a different C.G. offset obtained by shifting the pitch axis, before one was chosen for aerodynamic analysis. Natural frequencies, blade deformations, root loads, and 3D stresses were all studied. This work yields the following conclusions:

1. The selected blade design with the pitch axis at 40% chord has a factor of safety greater than two for all foreseeable test conditions, even with large oscillations created with blade cyclic.
2. Minimizing the C.G. offset, achieved by moving the pitch axis close to mid-chord is crucial to reducing the blade root loads and 3D stresses. The propeller moment is reduced by 30%-40%, and the blade in-plane lag force and flapping moment can be reduced by a factor of five.
3. Significant elastic pitch deformation is observed for all blade designs, with the exact behavior varying with collective. This phenomenon is due to the interaction of the trapeze effect and propeller moment, and must be included when modeling ultra-thin blades.
4. The blade control loads are significantly increased by the additions of oscillations through cyclic. This increase is primarily inertial and is due to the pitch-flap coupling from the C.G. offset. The high peak-to-peak means that fatigue must be considered when designing the pitch links.

The unusual nature of the blades and unique atmosphere means confidence in design and analysis will not mature without systematic validation. Validation for these unique blades is recommended in the form of blade stresses or strains. Two sets of pitch axis (at 40% and 25% chord) would be interesting to consider.

## ACKNOWLEDGMENTS

This work is supported partially by the NASA NIA Award No. 202060 with Haley Cummings as the Technical Point of Contact and Susan Gorton as the Sponsor. The support is gratefully acknowledged.

## REFERENCES

1. Savu, G., and Trifu, O., "Photovoltaic Rotorcraft for Mars Missions," 31st AIAA/ASME/SAE/ASEE Joint Propulsion Conference and Exhibit, July 10-12, 1995.
2. Young, L., and Edwin, W. A., "Vertical lift planetary aerial vehicles: Three planetary bodies and four conceptual design cases," the 27th European Rotorcraft Forum, Sep 11-14, 2001.
3. Datta, A., Roget, B., Griffiths, D., Pugliese, G., Sitaraman, J., Bao, J., Liu, L., and Gamard, O., "Design of a Martian autonomous rotary-wing vehicle," *Journal of Aircraft*, Vol. 40, (3), 2003, pp. 461-472. DOI: 10.2514/2.3141
4. Balaram, J., Daubar, I. J., Bapst, J., and Tzanetos, T., "Helicopters on Mars: Compelling Science of Extreme Terrains Enabled by an Aerial Platform." Ninth International, Ninth International Conference on Mars, July 2019.
5. Pipenberg, T. B., Keennon, T. W., Langberg, A. S., and Tyler, D. J., "Development of the Mars Helicopter Rotor System," American Helicopter Society 75th Annual Forum, May 2019.
6. Johnson, W., Withrow, S., Young, L., Malpica, C., Koning, W. J. F., Kuang, W., Fehler, M., Tuano, A., Chan, A., Datta, A., Chi, C., Lumba, R., Escobar, D., Bob Balaram, J., Tzanetos, T., and Grip, H. F., "Mars Science Helicopter Conceptual Design," Technical Report TM—2020–220485, NASA, 2020.
7. Chi, C., Lumba, R., and Datta, A., "Structural Design and Aeromechanical Analysis of a Next-Generation Mars Hexacopter Rotor," Vertical Flight Society's 77th Annual Forum, May 10-14, 2022.
8. Koning, W. J. F., Romander, E. A., and Johnson, W., "Optimization of Low Reynolds Number Airfoils for Martian Rotor Applications Using an Evolutionary Algorithm," AIAA Science and Technology Forum and Exposition, Jan. 2020.
9. Cummings, H., Perez Perez, N., Koning, W., Johnson, W., Young, L., Haddad, F., Romander, E., Balaram, J., Tzanetos, T., Bowman, J., Wagner, L., Withrow-Maser, S., Isaacs, E., Toney, S., Shirazi, D., Conley, S., Pipenberg, B., Datta, A., Lumba, R., Chi, C., Smith, K., Cornelison, C., Perez, A., Nonomura, T., and Asai, K., "Overview and Introduction of the Rotor Optimization for the Advancement of Mars eXploration (ROAMX) Project," Vertical Flight Society's Aeromechanics for Advanced Vertical Flight Technical Meeting, Jan 25-27, 2022.
10. Okamoto, M., Yasuda, K., and Azuma, A., "Aerodynamic Characteristics of the Wings and Body of a Dragonfly," *Journal of Experimental Biology*, Vol. 199, (2), 1996, pp. 281-294. DOI: 10.1242/jeb.199.2.281
11. Winslow, J., Otsuka, H., Govindarajan, B., and Chopra, I., "Basic Understanding of Airfoil Characteristics at Low Reynolds Numbers ( $10^4$ - $10^5$ )," *Journal of Aircraft*, Vol. 55, (3), 2018, pp. 1050-1061. DOI: 10.2514/1.C035075
12. Escobar, D., Chopra, I., and Datta, A., "High-Fidelity Aeromechanical Analysis of Coaxial Mars Helicopter," *Journal of Aircraft*, 2021, pp. 1-15. DOI: 10.2514/1.C035895
13. Datta, A., "X3D—A 3D Solid Finite Element Multi-body Dynamic Analysis for Rotorcraft," American Helicopter Society Technical Meeting on Aeromechanics Design for Vertical Lift, Jan. 2016.

14. Chi, C., Datta, A., Chopra, I., and Chen, R., “Three-Dimensional Strains on Twisted and Swept Composite Rotor Blades in Vacuum,” *Journal of Aircraft*, Vol. 58, (1), 2020, pp. 1–16.
15. Yamauchi, G., and Johnson, W., “Trends of Reynolds Number Effects on Two Dimensional Airfoil Characteristics for Helicopter Rotor Analyses,” Technical Report NASA-TM-84363, NASA, 1983.